frontiers | Frontiers in Materials

TYPE Original Research
PUBLISHED 05 September 2023
DOI 10.3389/fmats.2023.1234981

OPEN ACCESS

EDITED BY
Chang Boon Peng,
Nanyang Technological University,
Singapore

REVIEWED BY
Chin Wei Lai,
University of Malaya, Malaysia
Wael Abdelraheem,
Centers for Disease Control and
Prevention (CDC), United States

*CORRESPONDENCE
Yuan Zhao,
zhaoyuan@cczu.edu.cn
Liangzhong Li,
liliangzhong@scies.org

†These authors have contributed equally to this work and share first authorship

RECEIVED 05 June 2023
ACCEPTED 18 August 2023
PUBLISHED 05 September 2023

CITATION
Ji C, Yin H, Zhou M, Sun Z, Zhao Y and Li L (2023), Adsorption of total petroleum hydrocarbon in groundwater by KOH-activated biochar loaded double surfactant-modified nZVI.
Front. Mater. 10:1234981.
doi: 10.3389/fmats.2023.1234981

Adsorption of total petroleum hydrocarbon in groundwater by KOH-activated biochar loaded double surfactant-modified nZVI

Caiya Ji[1†], Hongyang Yin[2†], Meichun Zhou[3], Zhao Sun[2], Yuan Zhao[1*] and Liangzhong Li[4*]

[1]School of Environmental and Safety Engineering, Changzhou University, Changzhou, China, [2]Changzhou Keqing Environmental Protection Technology Co., Ltd., Changzhou, China, [3]Jiangsu Zhongwu Environmental Protection Industry Development Co., Ltd., Changzhou, China, [4]State Environmental Protection Key Laboratory of Environmental Pollution Health Risk Assessment, South Institute of Environmental Science, Ministry of Ecology and Environment, Guangzhou, China

Introduction: Crude oil and petroleum hydrocarbon contamination is commonly found in the soil and groundwater during the various processes of mining, processing, and utilization due to issues such as inefficient environmental management, random wastewater discharge, and storage tank leakage.To address this issue, we will use corn stalk biochar (SBC) and surfactants to improve the stability and chemical reactivity of nZVI, thereby enhancing its ability to remove pollutants, and explore the adsorption effect and mechanism of composite materials for petroleum hydrocarbons.

Methods: Modified corn stalk biochar (SBC) was synthesized through high-temperature carbonization and KOH activation. Subsequently, the iron/carbon composite PN-nZVI@SBC (PNMSBC) was prepared by loading nano zero-valent iron modified with dual surfactants, and it was adopted to adsorb total petroleum hydrocarbons(TPH) in groundwater. The physical and chemical properties, surface patterns, and elemental mapping of PNMSBC particles were analyzed using SEM, EDS, TEM,XRD, BET, and FTIR spectroscopy. Kinetics and isotherm tests were performed to evaluate the adsorption properties of the composites. TPH adsorption was dependent on ionic strength, initial TPH concentration, as well as pH. The adsorption mechanism combining XPS and EPR spectroscopy was explored.

Results: The characterization results by SEM and TEM showed that the particle size of nZVI particles modified by surfactants became smaller, and the dispersibility was enhanced. The characterization results by XRD and FTIR confirmed the successful preparation of the composites. The BET results showed that MSBC and PNMSBC were mesoporous structures. The characterization results indicated that Polyvinylpyrrolidone (PVP) and Sodium oleate (NaOA) inhibited the oxidation of nZVI while effectively improving its reactivity. The result of the experiments on adsorption showed that the removal of TPH by PNMSBC followed Freundlich isotherm and pseudo-second-order kinetic models, thus suggesting that the main adsorption processes comprise chemisorption and multilayer heterogeneous adsorption. The adsorption capacity of PNMSBC was increased by the abundance of macro and microporous structures. To be specific, a maximum Langmuir adsorption capacity (qm) was achieved as 75.26 g/g. The result of batch experiments indicated that PNMSBC continuously removed considerable TPH

under a wide pH range from 2 to 6. The adsorption mechanism of PNMSBC includes surface adsorption, oxidation, complexation, and electrostatic interaction.

Discussion: In brief, PNMSBC has a promising application for the adsorption of TPH in groundwater remediation.

KEYWORDS

nano zero-valent iron, corn stalk biochar, surfactant, total petroleum hydrocarbons, adsorption

1 Introduction

Groundwater, a significant freshwater supply, has been the primary source of drinking water in numerous regions (Arshad et al., 2020; Li R. et al., 2022). Total petroleum hydrocarbons (TPH) comprise a mixture of hydrocarbons and traces of other organic materials. TPH contamination has been widely detected in the soil and groundwater of crude oil mining and machining sectors for inefficient environmental management, arbitrary wastewater discharge, and storage tank leaks during oil extraction, processing, as well as utilization (Diraki et al., 2019). Petroleum hydrocarbon contaminants in the environment may be absorbed into the human body through inhalation and skin contact, which is likely to have teratogenic, carcinogenic, and mutagenic consequences (Smith et al., 2006). Several physical, chemical, and biological *in-situ* remediation techniques have been adopted to rehabilitate oil-contaminated locations. Yang et al. (Yang and Chen, 2020) prevented the dispersion of oil spillage in underground water using oil-absorbing barrier, oil-absorbing material, skimmer, and other equipment, with a maximum recovery rate of 30%. Poi et al. (Poi et al., 2018) restored TPH-contaminated groundwater through large-scale biofortification, which dropped from 1,564 $mg{\cdot}L^{-1}$–89 $mg{\cdot}L^{-1}$ in 32 days. Typically, the above technologies have significant operating and maintenance costs, require more time to fix, and may cause secondary pollution. The adsorption technique has been extensively used for its straightforward treatment method, cheap running expenses, and high repair effectiveness.

nZVI is capable of removing several types of pollutants from groundwater through chemical reduction and adsorption precipitation. It has aroused wide attention in the field of groundwater environmental restoration (Phenrat et al., 2016). nZVI cannot display adequate reactivity in terms of *in-situ* cleanup and groundwater storage for its propensity to agglomerate and low electron selectivity (Zhao et al., 2019). To address the aforementioned issues, materials such as resin, silica, and activated carbon are often employed to immobilize nZVI and boost its reaction efficiency (Gong et al., 2020). compared with the above nZVI immobilized materials, biochar is a readily available (Xu et al., 2018) and low-cost (Liu et al., 2019) raw material with a large specific surface area, a porous structure, and oxygen-containing compounds.

Coating nZVI particles with stabilizers is an additional method to enhance the dispersion and mobility of the particles in the solution. The spatial site resistance and electrostatic repulsion caused by different stabilizers (e.g., polymer electrolytes and surfactants) may prevent the aggregation of nZVI particles and distribute them evenly in solution, thus increasing the surface activity of nZVI (Zhao et al., 2016). A wide variety of stabilizers have been employed (e.g., nonionic surfactants, cationic surfactants, anionic surfactants, and amphoteric surfactants (Phenrat et al., 2009)). Polyvinylpyrrolidone (PVP) has become a widely used nonionic surfactant and shows numerous advantages (e.g., electrical properties, low price, and water solubility). Owing to the above qualities, PVP has extensively served as a dispersant in nanoparticle synthesis (Sakulchaicharoen et al., 2010). Moreover, PVP is capable of agglomerating with a variety of inorganic compounds for its unique strength and rigidity, such that it can apply to the manufacture of polymeric nanoparticles (Bubel et al., 2011; Zhou and Hu, 2017). Sodium oleate (NaOA) has been confirmed as a low-cost, environment-friendly anionic surfactant (Wang et al., 2018). NaOA significantly increases the colloidal stability of nZVI by improving nZVI mobility and overall reactivity and decreasing particle adherence to mineral surfaces (Lefevre et al., 2016). In this study, the two surfactants mentioned above will be utilized to increase the stability and chemical reactivity of nZVI, thus increasing its capacity to remove contaminants. In addition, the research on enhancing the reduction and remediation of TPH pollution in groundwater with carbon-coated nZVI by combining the solubilization and desorption properties of surfactants has not been reported.

This study aimed to develop stable, highly active iron/carbon composites by co-modifying PVP and NaOA to eliminate TPH from groundwater. To be specific, 1) PNMSBC was manufactured and characterized for precise physical and chemical properties; 2) the performance of PNMSBC for the adsorption of TPH was analyzed through batch experiment; 3) plausible mechanisms of PNMSBC for TPH elimination was proposed. This study lays a solid theoretical foundation for PNMSBC feasibility analysis of *in-situ* treatment of TPH-containing groundwater.

2 Materials and methods

2.1 Chemicals

Corn straw originated from a farmland in Changzhou, Jiangsu Province, China. The following chemicals were purchased from Sinopharm Chemical Reagent Co., Ltd, including diesel oil (TPH), ferrous sulfate heptahydrate ($FeSO_4{\cdot}7H_2O$), potassium hydroxide (KOH), sodium hydroxide (NaOH), sodium borohydride ($NaBH_4$), hydrochloric acid (HCl), ethanol (C_2H_6O), Polyvinylpyrrolidone (PVP), Sodium oleate (NaOA), potassium nitrate (KNO_3), sodium chloride (NaCl), calcium chloride ($CaCl_2$), sodium sulphate (Na_2SO_4), ammonium chloride (NH_4Cl), dipotassium hydrogen

phosphate (KH_2PO_4), tert-butanol (TBA), as well as p-benzoquinone (PBQ).

2.2 Preparation of materials

First, the corn straw was washed and dried, ground through a 20-mesh sieve and placed into a crucible. Subsequently, the samples pyrolyzed for 6 h at 300°C, 500°C, and 700°C (10°C/min^{-1}) underneath the flow of nitrogen. The raw biochar (expressed as RBC) was prepared by grinding through a 100-mesh sieve. Next, the RBC was immersed in KOH saturated solution for 24 h, filtered and dried, placed in a crucible, and then heated to 750°C (10°C/min^{-1}) for 2 h underneath the flow of nitrogen. Afterward, the pyrolyzed products were diluted with HCl for purification till the pH reached 7.0 and the products evaporated at 60°C. The acquired biochar was termed SBC.

The method employed to synthesize SBC loaded double surfactant-modified nZVI (PNMSBC) was similar to an early published study (Xu et al., 2022). This product is typically produced using the liquid phase reduction method. Subsequently, 2.78 g $FeSO_4{\cdot}7H_2O$ and 0.5 g SBC were first dissolved in 50 mL ultra-pure water in a three-necked flask. Moreover, N_2 was purged to remove any dissolved O_2. Next, 0.1g PVP and NaOA were added and completely dissolved through magnetic agitation. Afterward, 1.51 g $NaBH_4$ was added and magnetically agitated for 30 min, at which point the formed blackish particles were distinct from the liquid state. Lastly, the final particles were identified as PNMSBC. Furthermore, SBC-loaded nZVI composite (MSBC) can be synthesized using the PNMSBC preparation method without the addition of PVP and NaOA.

2.3 Analytical methods

The elemental compositions of all samples were measured using an elemental analyzer (Vario EL III Element Analyzer, Germany). The surface area, pore volume and pore size distribution were measured by N_2 adsorption/desorption method at liquid temperature (77 K) (ASAP2460 physical adsorption instrument). The zero point charge (pH*zpc*) of MSBC and PNMABC were measured using zeta potential analyzer (ELSZ-2000ZS, Japan). The crystallographic structure and phase composition characteristics were analyzed by X-ray diffractometer (D/MAX-2500, Japan). The surface morphology and composition were detected by Scanning electron microscope (SEM, Hitachi, Japan) images along with a HORIBA EX-350 EDS detector. The surface functional groups were identified by FITR (Nicolet FTIR 6700, America) in the 4,000–400 cm^{-1} spectral range. The content of diesel oil (TPH) was examined using GC–FID (GC9790, America) (Desalegn et al., 2018; Bolade et al., 2021).

2.4 Adsorption experiments

2.4.1 Kinetic adsorption experiment

The TPH adsorption capacities of RBC, SBC, MSBC, and PNMSBC were examined through the batch sorption process. to investigate adsorption kinetics, 15 mg of adsorbent and 0.529 mL diesel oil (initial concentrations 3 g/L) were added into 250 mL conical flasks, and the adsorption was conducted at natural pH. The samples were oscillated at a frequency of 150 rpm at 291 K. The length of adsorption was 80 min, and the samples were extracted every 10 min. The TPH content was examined using GC–FID. The experimental results were interpreted using Pseudo-first-order, Pseudo-second-order, intraparticle diffusion, and Bangham channel diffusion models. Eqs 1–4 showed expressions.

$$\text{Pseudo} - \text{first} - \text{order model: } q_t = q_e\left(1 - e^{-k_1 t}\right) \quad (1)$$

$$\text{Pseudo} - \text{second} - \text{order model: } t/q_t = 1/k_2 q_e^2 + t/q_e \quad (2)$$

$$\text{Intraparticle diffusion model: } q_t = k_i t^{1/2} + C \quad (3)$$

$$\text{Bangham channel diffusion model: } \lg q_t = \frac{1}{m}\lg t + \lg k \quad (4)$$

Where q_t (g·g^{-1}) represents the adsorption capacity at t moment; q_e (g·g^{-1}) denotes the equilibrium adsorption density; k_1, k_2 and k_i are adsorption rate constants; C denotes a constant linked to the thickness of boundary layer; m and k represent the constants determined by the graph of $\lg q_t$ *versus* $\lg_t$.

2.4.2 Isothermal adsorption experiment

150 mL of 1–10 g/L diesel oil solution was emptied into 250 mL conical flasks with 15 mg of adsorbent and oscillated for 60 min at 150 rpm and 291 K. The TPH concentration was examined using GC–FID. The experimental data were assessed using Langmuir, Freundlich, Temkin, and Redlich-Peterson models. The expressions are presented in Eqs 5–8.

$$\text{Langmuir model: } q_e = q_m K_1 C_e / (1 + K_1 C_e) \quad (5)$$

$$\text{Freundlich model: } q_e = K_f C_e^{1/n} \quad (6)$$

$$\text{Temkin model: } q_e = RT/b_t \ln(K_t C_e) \quad (7)$$

$$\text{Redlich} - \text{Peterson model: } q_e = AC_e/1 + BC_e^g \quad (8)$$

Where C_e (g·L^{-1}) represents the equilibrium adsorption density, K_l (L·g^{-1}) symbolizes Langmuir adsorption coefficient, q_m represents adsorption capacity; K_f and 1/n represents the adsorption coefficient and nonlinear coefficient in Freundlich equation respectively; R (8.314 Jmol·K^{-1}) represents the absolute temperature, T(K) represents the universal gas constant; A, B and g are Redlich-Peterson constants ($0 < g < 1$).

2.4.3 Batch experiments on the adsorption process

TPH adsorption experiments were performed on all adsorbents through intermittent adsorption. Unless otherwise stated, all experiments were performed in a thermostatic oscillator, and adsorbent adsorption experiments were performed in a 250 mL conical flask containing 150 mL TPH solution (the initial pH was not adjusted) and 15 mg adsorbent. Except for special requirements, the concentration of TPH solution is 3 g/L, and other experimental conditions are consistent with the above. The effect of pH was studied by adjusting the pH of TPH solution in the range of 2–11. The initial TPH concentrations ranged from 1 to 9 g/L to examine their effect on adsorption. 0–0.1 M NaCl, $CaCl_2$, KNO_3, NH_4Cl, KH_2PO_4, and Na_2SO_4 were additionally added to explore the effects of NH_4^+, Ca^{2+}, Cl^-, NO_{3-}, PO_4^{3-}, and SO_4^{2-}. specimens The TPH concentration of samples was investigated through GC-FID. The

10.3389/fmats.2023.1234981

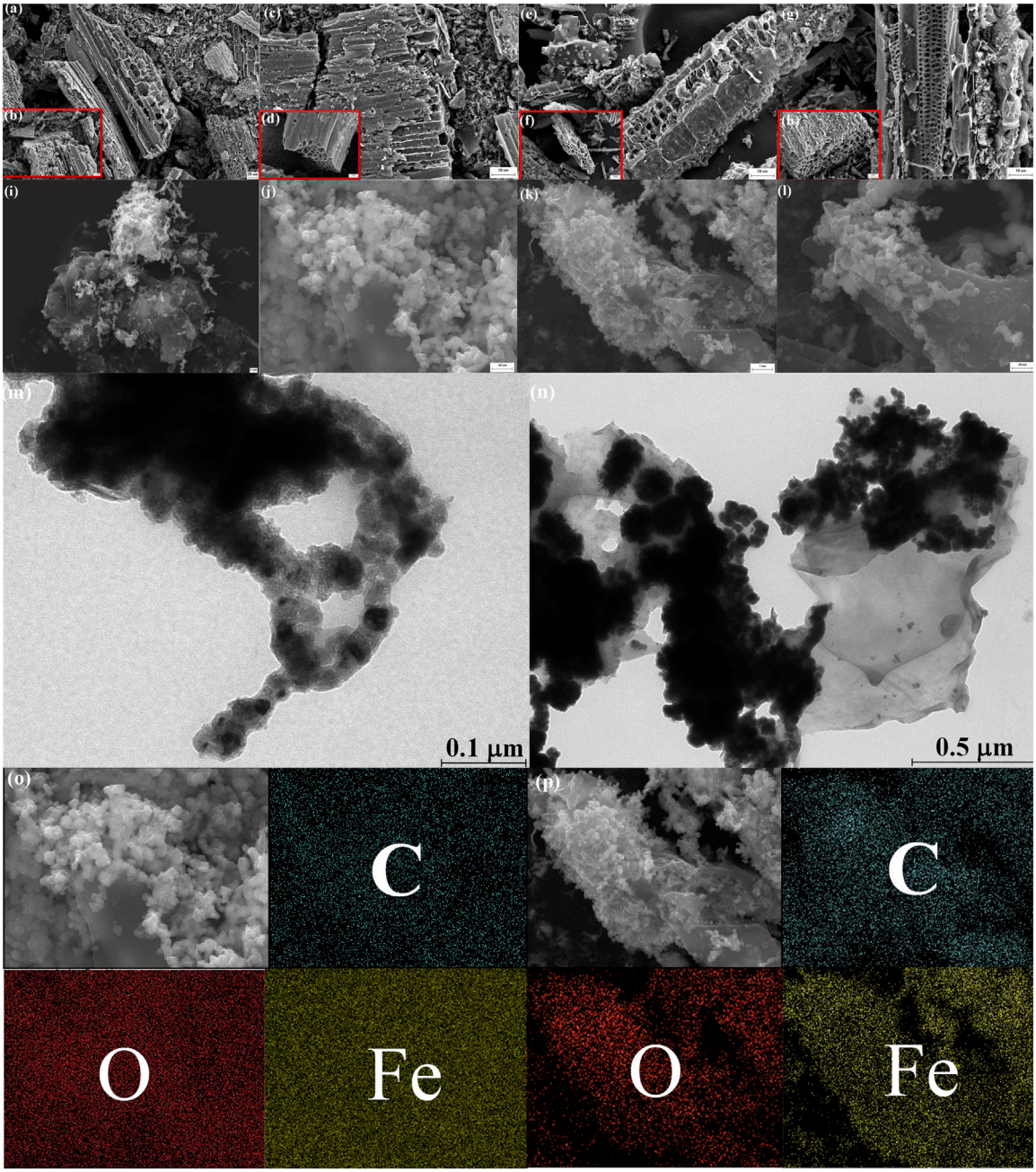

FIGURE 1
SEM images of **(A, B)** RBC; **(C, D)** SBC-300; **(E, F)** SBC-500; **(G, H)** SBC-700; **(I, J)** MSBC; **(K, L)** PNMSBC and TEM of **(M)** MSBC; **(N)** PNBSBC and Mapping of **(O)** MSBC; **(P)** PNMSBC.

TPH adsorption on adsorbent at time t (q_t, $g{\cdot}g^{-1}$) was obtained using Eq 9.

$$q_t = (C_0 - C_t) \times V/m \tag{9}$$

Where C_0 ($g{\cdot}L^{-1}$) and C_t ($g{\cdot}L^{-1}$) denote TPH concentrations at initial and t (min), respectively. Moreover, m (g) and V (L) represent the mass of adsorbent and the volume of reaction solution, respectively.

2.5 Reusability

MSBC and PNMSBC after adsorption were added to 0.5 M NaOH solution for recovery. The sample was agitated at 353 K for 1 h and then replenished with distilled water for another 1 h for full desorption. Subsequently, the regenerated adsorbent samples were rinsed and then dried. Furthermore, the adsorption regeneration capacity and stability of MSBC and PNMSBC regeneration procedures were investigated.

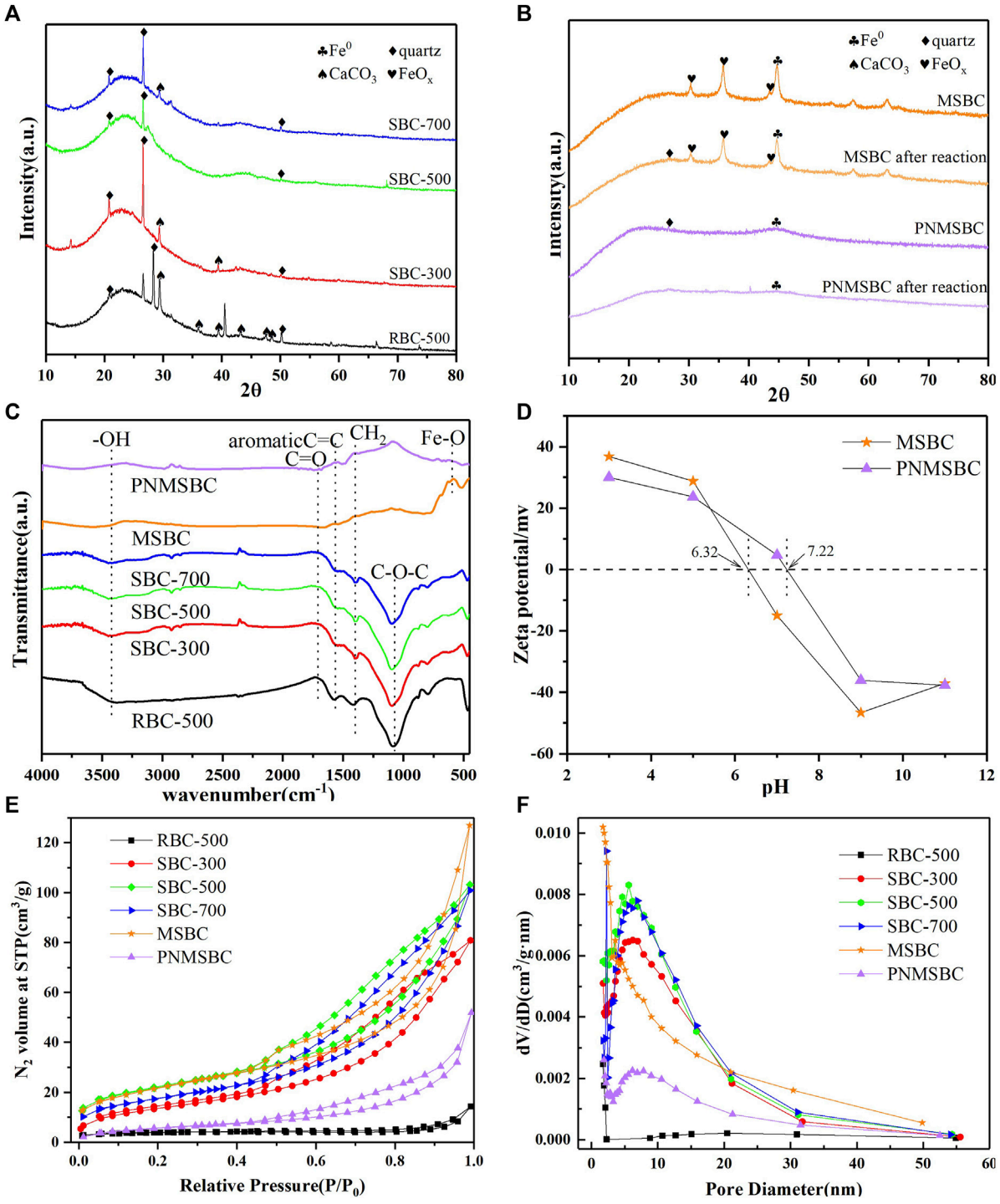

FIGURE 2
XRD patterns of **(A)** RBC, SBC; **(B)** MSBC, PNMSBC and FTIR spectroscopy of **(C)** RBC, SBC, MSBC, PNMSBC and Zeta potential of **(D)** MSBC, PNMSBC and N_2 adsorption-desorption curves **(E)**, pore size distribution **(F)** of RBC, SBC, MSBC, PNMSBC.

3 Results and discussion

3.1 Characterization of RBC, SBC, MSBC and PNMSBC

The morphology of the RBC, SBC, MSBC, and PNMSBC samples were studied through SEM and TEM (Figure 1). As depicted in Figures 1A,B, RBC had a smooth surface and a considerable number of regular hollow channels, and combined with the results of the pore size distribution curve in Figure 2F), the pore size range of RBC is mostly distributed in the range of 0–4 nm, which was largely concentrated in the micropore and mesopore range. Numerous pores were identified on the KOH-modified biochar (Figures 1C–H) and then validated through N_2

adsorption-desorption analysis (Supplementary Table S2). The surface pore size of SBC became increasingly larger with the increase of the carbonization temperature, and fracture and collapse occurred, thus indicating that a dense uneven structure was formed. As depicted in Figures 1I–L, the synthesized nZVI particles on MSBC were spherical in shape, and chain-like aggregates were formed on the particles, which were evenly disseminated across the SBC surface due to magnetic interactions. There were two reasons for the improved dispersion of PVP and NaOA modified nZVI. First, surfactants are capable of decreasing the agglomeration through high electrostatic repulsion (Eljamal et al., 2020). On the other hand, surfactants are likely to significantly increase the steric-hindrance effect and reduce the magnetic forces, van der Waals forces and surface tension (Ogawa and Kawase, 2021). The particle sizes of nZVI were obtained as 25–35 nm and 7–16 nm based on the TEM characterization findings of MSBC and PNMSBC in Figures 1M, N, respectively. The inclusion of PVP and NaOA in synthesis led to the modified crystalline structure, the lowered particle size by inhibiting aggregation, as well as a large surface area for enhanced catalytic properties. The comparison of TEM images indicated that PNMSBC exhibited a core-shell or egg yolk like structure, and the formation of core may be attributed to PVP covering, and the eggshell was attributed to Fe^0 (Idrees et al., 2021). At the same time, surfactant modification removed thin outer layer of nZVI. The outer layer may be an oxide layer, explaining the lowered oxide concentration of PNMSBC (Supplementary Table S2) (Liu H. et al., 2022). The element mapping analysis of MSBC and PNMSBC was conducted by Figures 1O, P, and the distribution of C, O and Fe was indicated. The result indicated that Fe element was uniformly distributed across the SBC to synthesize MSBC and PNMSBC composite.

The XRD patterns of different material exhibited broad peaks were identified at 2θ angles 20.8°, 26.6° and 50.2° in Figures 2A, B, which were recognized as quartz in the structures of RBC, SBC, MSBC, and PNMSBC, for whom the degree of expansion was correlated with an amorphous structure (Hussain et al., 2017). The faint peaks at 29.4°, 35.9°, 39.4°, 43.1°, 47.5°, 48.5° belonged to the presence of $CaCO_3$ in RBC and SBC structures (Dai et al., 2020). Nevertheless, the peaks of $CaCO_3$ on SBC were less than those on RBC, thus suggesting that KOH facilitates $CaCO_3$ elimination. XRD pattern of MSBC and PNMSBC samples are presented in Figure 2B. Strong peaks were identified at 44.9° after nZVI immobilization, consistent with the (110) plane of α-Fe^0. After the reaction with TPH, the quartz diffraction peak of PNMSBC was significantly weakened, thus suggesting that the inherent crystal structure of biomass carbon is not stable and easily collapsed under the action of the reaction. The diffraction peak of Fe^0 decreased or even disappeared as the nano-zero-valent iron was consumed by the reaction and entered the solution into Fe^{2+} or Fe^{3+}. MSBC showed faint diffraction peaks at 2 = 30.2°, 35.7° and 43.5°, thus confirming the presence of Fe_2O_3 and Fe_3O_4 (Zhu et al., 2018).

The FTIR spectra for different samples were performed between 400 and 4,000 cm^{-1} (Figure 2C). -OH stretching vibration peak was identified as 3,420 cm^{-1}, thus indicating that the composites exhibited considerable oxygen-containing structural features (Zhang S. et al., 2020). The peak at 1710 cm^{-1} was generated through C=O ester stretching and O-H stretching (Gan et al., 2015). The C=C, CH_2 and C-O-C stretching vibrations identified at 1,499, 1,403, and 1,100 cm^{-1} were likely to belong to the presence of aromatic ring structures. The peak at 592 cm^{-1} in MSBC and PNMSBC corresponded to the Fe-O tension and deformation vibration (Su et al., 2016). FTIR results indicate that SBC loaded surfactant-modified nZV increases the surface functional groups of PNMSBC.

MSBC and PNMSBC achieved the zero point charge (pH*zpc*) of 6.32 and 7.22, respectively, and their surfaces were positively charged once the pH fell below pH*zpc* (Figure 2D). The electrostatic repulsion force decreased with the increase of pH from 3 to 7, leading in a rise in TPH elimination efficiency. The maximum MSBC and PNMSBC TPH elimination efficiency was obtained at pH 6 to 7. The adsorbent surface had a negative charge when the solution pH exceeded pH*zpc* (Jang and Kan, 2019a). With the increase of pH, the negative charge of adsorbents and TPH species led to charge separation and poor adsorption, thus reducing TPH removal efficiency. Furthermore, iron oxide/hydroxide precipitates (e.g., $Fe(OH)_3$ and Fe_3O_4) developed readily on iron material surfaces in an alkaline environment, thus reducing TPH removal efficiencies (Huang et al., 2019). Electrostatic repulsion force may not facilitate the removal of TPH by MSBC and PNMSBC at solution pH values of 6 and 7, whereas hydrogen bonding, pore filling, and π-π interaction played a certain role in TPH adsorption (Xu et al., 2022).

Supplementary Table S2 lists the properties of RBC, SBC, MSBC, and PNMSBC. The comparison of the carbon content of the SBC to that of the RBC indicated that the KOH-activated treatment facilitated the graphitization of RBC (Qin et al., 2022). Moreover, the reduction in C, H and N contents in MSBC and PNMSBC may arise from Fe addition. The atomic ratios (O + N)/C, O/C, and H/C represent polarity, hydrophilicity, and aromaticity, respectively (Al-Wabel et al., 2013). The lower the H/C value, the greater the value of (O+ N)/C will be, and the higher the polarity and hydrophilicity will be (Takeuchi et al., 2008). Similar results of SBC and PNMSBC were obtained, which were more aromatic and hydrophobic than RBC and MSBC.

Nitrogen adsorption-desorption experiments were performed to characterize the features of sample textures. The corresponding results are presented in Figures 2E, F; Supplementary Table S2. The adsorption-desorption isotherms (Figure 2E) were all type IV isotherms and H_3 hysteresis loops in accordance with the IUPAC adsorption isotherm classification, thus indicating that a porous structure was formed in the above materials. When N_2 molecules were adsorbed on the mesoporous layer, the sample isotherms increased at low P/P_0 (0.0-0.5). The mesoporous nature of the materials led to a dramatic spike between 0.5 and 1.0 relative pressure. Figure 2F presents the salient pore size trends. SBC exhibited greater numbers of micropores and mesopores than RBC. Compared with the micropore and mesopore distributions of SBC with three different carbonization temperatures, SBC-500 > SBC-700 > SBC-300, thus indicating that 500°C carbonizations most significantly enhanced RBC pore structure. As depicted in Supplementary Table S2, the BET surface area of SBC (76.692 m^2/g) was greater than that of RBC (13.247 m^2/g), whereas the BJH pore volume was 10 times that of RBC, thus

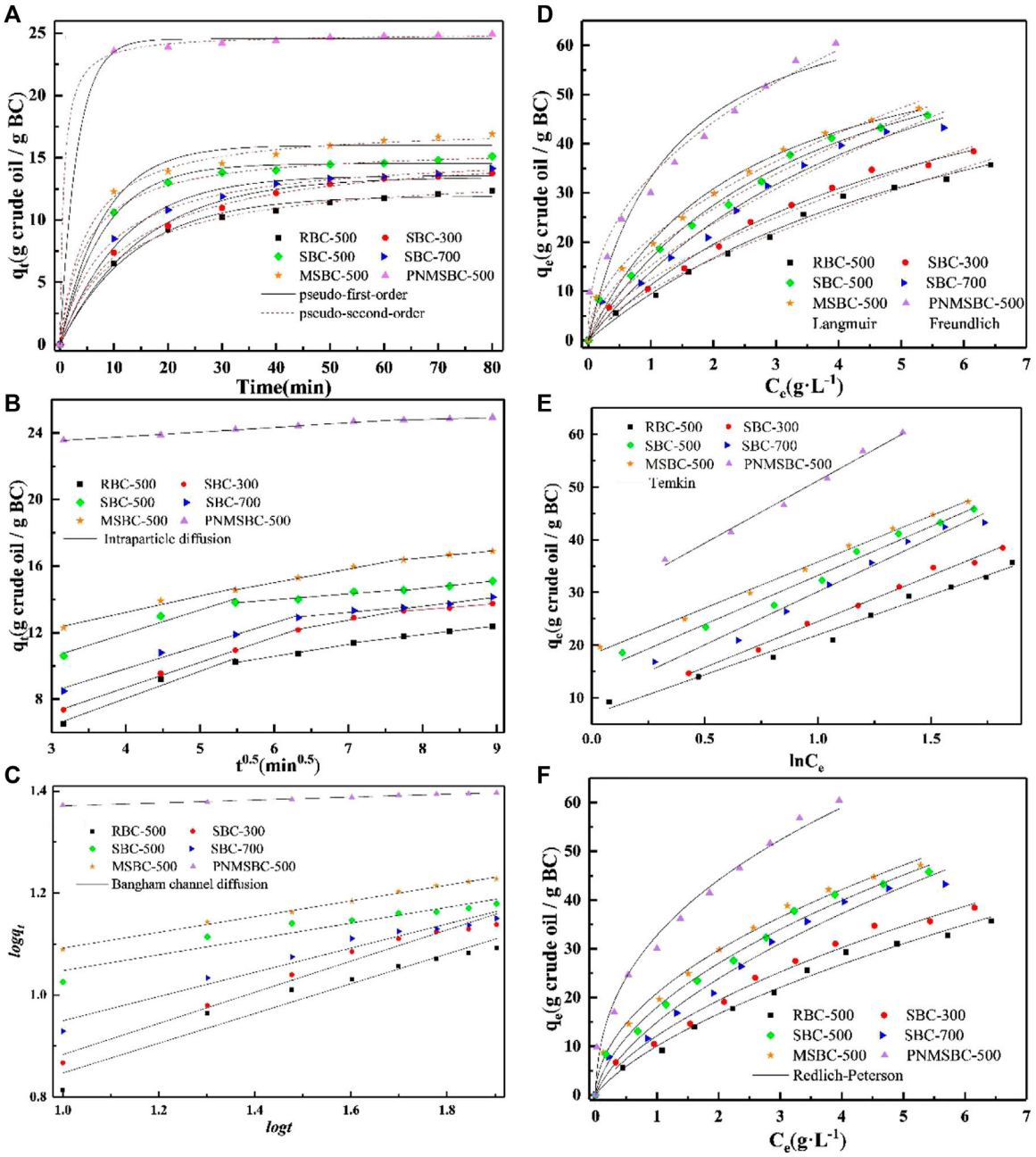

FIGURE 3
Adsorption kinetic of pseudo-first-order plots and pseudo-second-order plots **(A)**, intra-particle diffusion plots **(B)**, Bangham plots **(C)** for TPH adsorption by RBC, SBC, MSBC and PNMSBC ([TPH]$_0$:3 g/L; [RBC]$_0$/[SBC]$_0$/[MSBC]$_0$/[PNMSBC]$_0$: 0.1 g/L; T: 291 K; t: 80 min), and adsorption isotherm of Langmuir plots and Freundlich plots **(D)**, Temkin plots **(E)**, Redlich-Peterson plots **(F)** for TPH adsorption by RBC, SBC, MSBC and PNMSBC ([TPH]$_0$: 1–10 g/L; [RBC]$_0$/[SBC]$_0$/[MSBC]$_0$/[PNMSBC]$_0$: 0.1 g/L; T: 291 K).

suggesting effective alteration. The BET surface area and average particle size of MSBC were not significantly changed than those of SBC. Combined with SEM analysis, it was possible that nZVI particles were evenly disseminated across the SBC surface due to magnetic interactions and did not enter the macro and microporous structures (Neeli and Ramsurn, 2018). The BET surface area of PNMSBC specific (21.303 m^2/g) was smaller than that of the MSBC (77.176 m^2/g), probably because the synthesized nZVI particles on the MSBC exhibit a chain-like morphology with numerous nanoscale particles. In contrast, PNMSBC comprised different sizes and well-shaped spheres (Li et al., 2022b). The larger average particle size of PNMSBC than MSBC reveals that PNMSBC exhibits a greater adsorption capacity. In addition, the pore size of PNMSBC is mainly distributed in the range of 0–10 nm, which can be determined that PNMSBC has rich mesoporous structure, accompanied with a large surface area and narrow pore size distribution. Further research is needed for the existence of microporous structure.

3.2 Adsorption kinetics

Compared with previous studies showed in Supplementary Table S3, TPH adsorption in this study need less time to reach equilibrium and the removal rate is higher. Figure 3A depicts the pseudo-first order and pseudo-second order kinetics of TPH elimination. Supplementary Table S1 displays the computed outcomes of the two models. The pseudo-second-order model fit adsorption better than the pseudo-first-order model (0.995–0.999 vs. 0.978–0.998) (Supplementary Table S1), indicating that the decisive phase could be chemical sorption (Zeng et al., 2019). In general, the pseudo-first-order model: mainly assumes that the diffusion step dominates the adsorption process. The pseudo-second-order model assumes that the chemisorption mechanism controls the adsorption rate. Two mechanisms usually occur in the adsorption process, and the slightly higher R^2 of pseudo-second-order model indicates the decisive phase could be chemical sorption (Wang et al., 2021). When the adsorption approached equilibrium, the equilibrium adsorption capacity of TPH by adsorbent was arranged as follows: PNMSBC > MSBC > SBC-500 > SBC-700 > SBC-300 > RBC. Approximately 48.0% (MSBC) and 80.6% (PNMSBC) of the total crude oil adsorbed onto adsorbent at equilibrium (60 min) was rapidly absorbed during the first contact duration of 30 min. The inclusion of free-active sites on the surface of the adsorbent may explain this occurrence of a greater initial adsorption rate. However, after 30 min of contact time, the adsorption rate practically stayed constantly attributable to the adsorbent surface becoming saturated with crude oil and achieving equilibrium. The intraparticle diffusion model determines the diffusion mechanism and rate-limiting step in adsorption.

The estimated intraparticle diffusion model curves comprise of three linear parts and do not traverse origin, showing TPH adsorption is a multistep process (Figure 3B) (Qu et al., 2021). TPH transfers swiftly from water to adsorbent, hence the first stage of adsorption happens fast. In the second step, the adsorption rate slowed due to TPH intraparticle diffusion in material pores. In the last stage, adsorption achieved equilibrium gradually. Compared with the rate constant of each stage, k1 is much greater than the others, indicating that film diffusion is the rate-limiting phase during the whole adsorption process. The Bangham channel diffusion model illustrates the real rate-limiting phase. The high linear coefficients of R^2 values for Bangham model indicate that channel diffusion behavior has a major impact in adsorption (Figure 3C).

3.3 Adsorption isotherms

Figure 3D shows that q_e values rose with C_e values, which is generally attributed to a stronger driving force and adsorption contact area. The R_L was found between 0 and 1 when the initial concentration of TPH was between 1 and 10 $g{\cdot}L^{-1}$. Consequently, it was established that the absorbent had a high affinity for TPH and that the adsorption process happened quickly (Gao et al., 2022). R_L has an inverse correlation with K_L, and the smaller R_L is conducive to adsorption. It can be seen from Supplementary Table S1 that the K_L value of PNMSBC (0.787) is higher than that of MSBC (0.409), so PNMSBC has a better adsorption effect on TPH. There was no significant increase in q_m for RBC, SBC, MSBC and PNMSBC, which might be because the modification method increased the adsorption rate of the adsorbent, but BC still dominated the adsorption amount. The correlation coefficient (R^2) of Freundlich model for MSBC was 0.994, which was higher than the 0.983 of Langmuir model. The R^2 value of Freundlich model (0.985) for PNMSBC was greater than that of Langmuir model (0.922). The substantial correlation coefficient fit the Freundlich model more accurately, suggesting that the adsorption of TPH was multilayer heterogeneous. In this work, isotherms with $1/n < 1$ imply preferential adsorption (Dragan et al., 2014), this means that all TPH is readily adsorbable for all adsorbents. As seen in Figure 3E, in the application of the Temkin isotherm model, demonstrating that strong intermolecular forces play a significant role in the TPH adsorption process. As adsorption rises, the total heat of adsorption decreases (Zeng et al., 2022). The adsorption of TPH on adsorbent could be better described by Redlich-Peterson isotherm model (Figure 3F), which incorporates both the Langmuir and Freundlich isotherm models (Li et al., 2022c). All B values were greater than 1, suggesting that the analyzed system tends to conform to the Freundlich -type mechanism. From these results, we infer conclude that the process mostly included multilayer heterogeneous adsorption (Liu T. et al., 2022).

3.4 Effects of ionic strengths, initial TPH concentration and pH on TPH adsorption

Figure 4A presents the effect of the types and concentrations of different coexisting ions on the removal of TPH by PNMSBC. The minor effects of Na^+, Ca^{2+} and SO_4^{2-} ionic on TPH adsorption were primarily attributed to their weaker affinity for Fe than TPH. Nevertheless, SO_4^{2-} removed iron oxide and hydroxide, thus removing the passivation layer and expanding the number of active sites on the surface of nZVI (Shang et al., 2017). PO_4^{3-}, NO_3^- and Cl^- significantly limited TPH removal. One potential reason for TPH inhibition is that it competes with TPH on the PNMSBC surface for reaction sites (Wang et al., 2013). However, the concentrations of the above ions were significantly higher than in natural waters, thus indicating that PNMSBC exhibited a significant affinity for TPH in the presence of most other anions. The above analysis reveals that PNMSBC has promising practical applications.

Figure 4B shows the effect of the initial TPH concentration. The adsorption capability of the four substances increased as the initial concentration of TPH increased. PNMSBC shows a much higher removal capacity than TPH. With the increase of the initial TPH concentration, the driving force between TPH and adsorbents increased, correlated with the increase of the adsorbent surface active site occupancy. Furthermore, the conclusion derived from the above studies reveals that the active sites on the surface of PNMSBC may be exploited efficiently at a high TPH concentration, thus confirming that PNMSBC is highly reactive.

The solution pH value might affect adsorption by affecting sample surface charges and TPH molecules (Mittal et al., 2012). The pH of TPH adsorption tests varied from 2.0 to 11.0. As depicted in Figure 4C, TPH adsorption increased from pH 2 to 6, where the highest adsorption capacity of PNMSBC was 27.4 g/g at pH value of 6 and subsequently dropped from pH 7 to 11. Thus, TPH removal from a slightly acidic to a neutral solution proved advantageous. Under identical conditions, the activity of PNMSBC to remove TPH

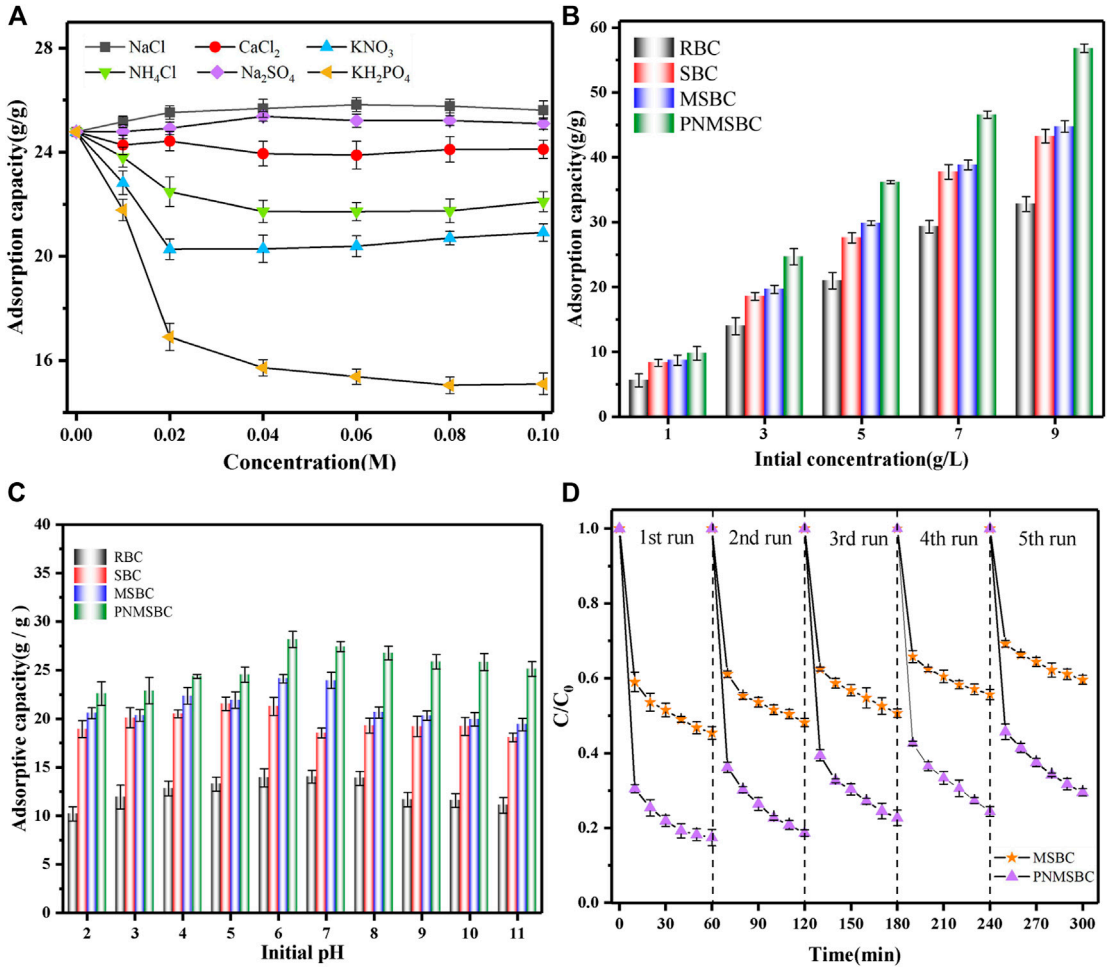

FIGURE 4
The influence factors on the removal of TPH: **(A)** coexisting anions ($[TPH]_0$: 3 g/L; $[PNMSBC]_0$: 0.1 g/L; t: 80 min; T: 291 (K); **(B)** initial TPH concentration ($[RBC]_0$/$[SBC]_0$/$[MSBC]_0$/$[PNMSBC]_0$: 0.1 g/L; t: 80 min; T: 291 (K); **(C)** Effect of initial pH for the removal of TPH ($[TPH]_0$: 3 g/L; $[RBC]_0$/$[SBC]_0$/$[MSBC]_0$/$[PNMSBC]_0$: 0.1 g/L; t: 80 min; T: 291 (K); **(D)** Reusability test of MSBC and PNMSBC.

was better than that of MSBC. The good removal of TPH under acidic conditions may be attributed to the fact that the presence of large amount of H^+ facilitates the corrosion and oxidation of Fe^0, thus contributing to the reduction of TPH (Huang J. et al., 2022). The result suggests that alkaline surroundings do not apply to the adsorption of TPH by nZVI and the reduction of TPH by Fe0, principally because the quick formation of metal anion of nZVI hinders the interaction of nZVI with TPH (Liu et al., 2021).

3.5 Mechanism of TPH removal

3.5.1 XPS analysis before and after adsorption

High resolution X-ray photoelectron spectroscopy of C1*s*, O1*s* and Fe2*p* was investigated on MSBC and PNMSBC to determine the changes in chemical conditions of C, O and Fe before and after adsorption, so as to clarify the involvement of nZVI in the adsorption process. Figure 5 depicts the complete survey spectra of MSBC and PNMSBC before and after reaction and the narrow region spectra of the elements presented in the figure.

Figure 5B presents the C1*s* high resolution spectra of MSBC before and after adsorption. The spectra of carbon were fitted with four peaks, including C-C of 284.8 eV, C-O-C of 285.55 eV and O-C=O of 289.08 eV (Zhu et al., 2019). The relative content of the above functional groups varied after TPH adsorption. C-C content increased from 43.10% to 45.75%, C-O-C content increased from 38.79% to 47.17%, whereas O-C=O content declined from 18.10% to 7.08%. The above modifications also appeared in PNMSBC (Figure 5F) though the pattern was distinct from that of MSBC. C-C content was reduced from 47.62% to 42.51%, C-O content grew from 40.95% to 48.31%, and O-C=O content declined from 11.43% to 9.18%, thus diminishing their photoelectronic spectral intensity. The above data indicated that the relative concentration of C-C changed after MSBC and PNMSBC absorbed TPH. Iron precipitation may arise continually on PNMSBC throughout the adsorption process, thus largely obscuring the C-C surface and decreasing the relative content. Iron oxides may dissolve during MSBC adsorption, thus resulting in constant exposure to the C-C surface.

10.3389/fmats.2023.1234981

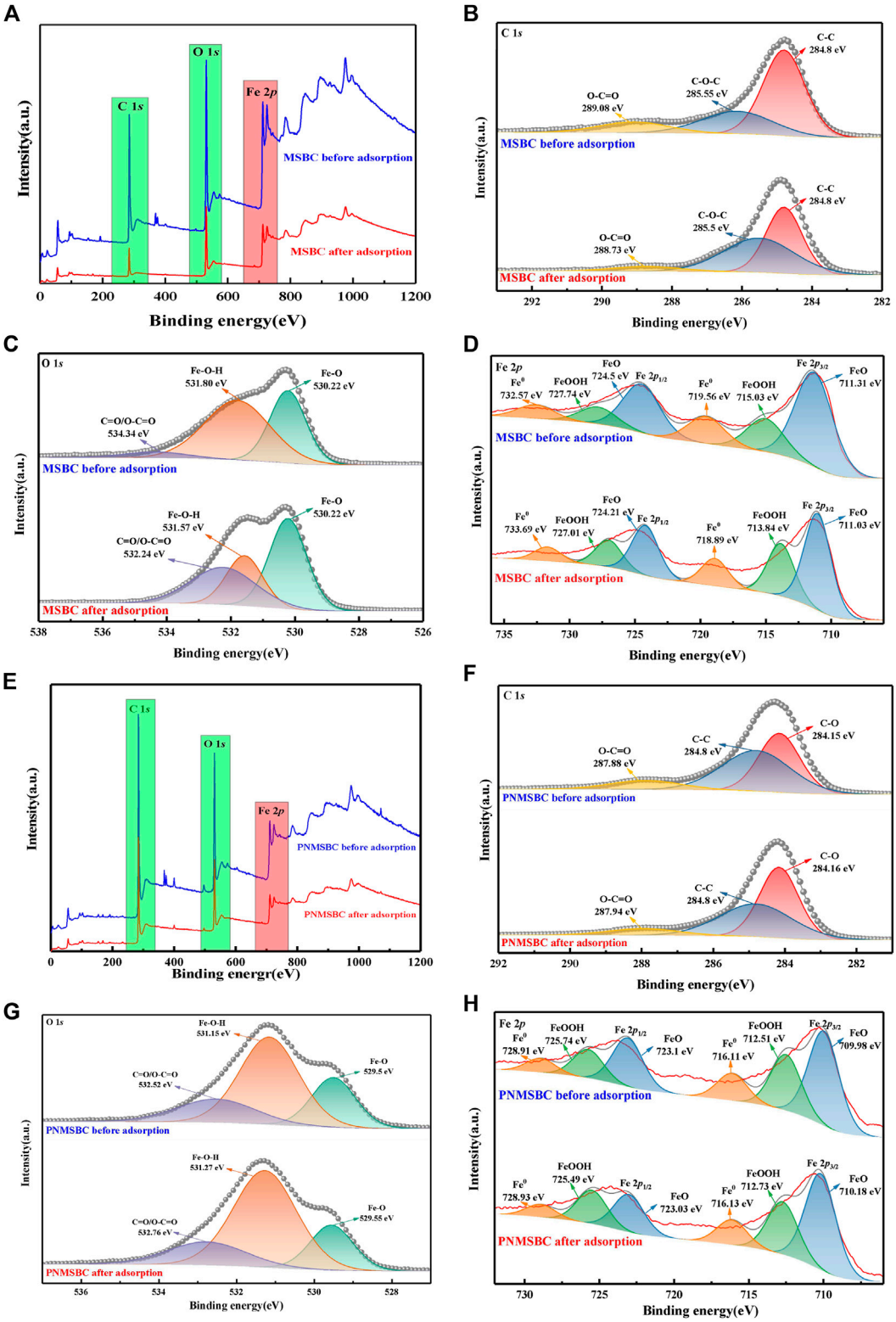

FIGURE 5
XPS patterns of survey spectra, C1*s*, O1*s*, Fe2*p*, for MSBC **(A–D)** and PNMSBC **(E–H)** before and after reaction.

Figures 5C, G present O1*s* high resolution spectra of MSBC and PNMSBC before and after adsorption. The peaks at 530.22 eV, 531.8 eV and 534.34 eV corresponded to Fe-O, Fe-O-H and C=O or O-C=O, respectively (Li et al., 2020). The peaks of Fe-O may belong to the oxidation process of nZVI nanoparticles to generate iron oxide shells or to interactions with functional groups on the surface

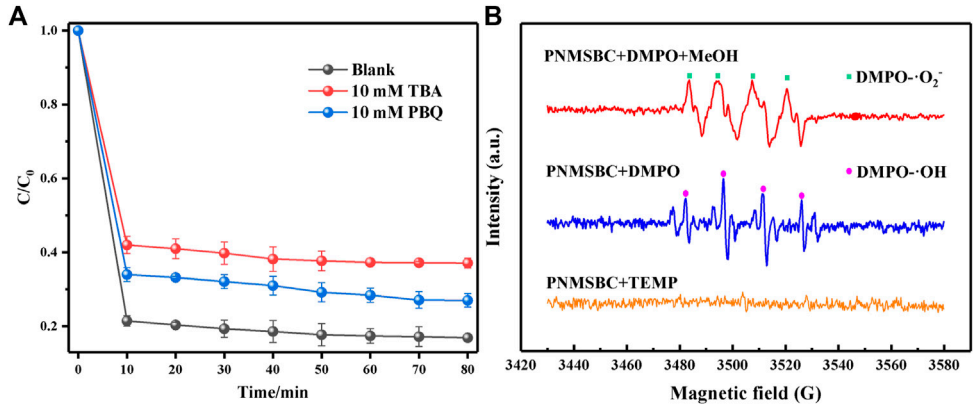

FIGURE 6
Free radical identification in PNMSBC: **(A)** influences of PBQ and TBA on TPH degradation; **(B)** EPR of PNMSBC (5%, v/v).

(e.g., -COOH and -C=O) to form -COOFe/-OFe (Qiu et al., 2011; Wu et al., 2018). Fe-O-H peaks indicated the presence of iron hydroxide or hydroxyl oxide in the shell of nZVI (Sarathy et al., 2008). The reason for the above result is that nZVI reacts with water to produce OH-, thus reacts with metal ions in the solution to form hydroxide precipitates (e.g., $Fe(OH)_3$) (Tosco et al., 2014; Cai et al., 2019). It is therefore confirmed that oxygen-containing functional groups eliminate TPH (Ma et al., 2022).

Figures 5D, H displayed the Fe2*p* high resolution spectra of MSBC and PNMSBC before and after adsorption. Fe^0, FeO and FeOOH make up 17.52%, 60.87% and 21.61% of surface iron atoms before adsorption. After adsorption, the ratio of FeOOH increased from 21.61% to 29.77%, consistent with the XRD results, thus suggesting the occurrence of oxidation (Cai et al., 2019). Inorganic compounds and iron oxides/hydroxides may co-precipitate during oxidation in accordance with existing research. Corrosion of nZVI leads to the production of an oxide layer (Tian et al., 2020). The existence of high valence iron species coupled with O1*s* spectra, and XRD analysis indicated that nZVI was covered by a layer of iron oxide (Sun et al., 2006).

3.5.2 Reactive species identification

Experiments on free radical quenching were performed to determine the free radical species in PNMSBC. Tert-butanol (TBA) and p-benzoquinone (PBQ) were employed as the quenching agents for •OH and $•O_2^-$. As depicted from Figure 6A, 80 min after adding 10 mM TBA and PBQ to the PNMSBC reaction solution, the TPH removal rate decreased from 84% to 63% and 73%, respectively. The above findings suggest that •OH and $•O_2^-$ free radicals play a certain role in the TPH adsorption process. The quenchers of singlet oxygen ($^1O_2$) (e.g., sodium azide) usually consume free radicals, thus making it difficult to determine the function of $^1O_2$ in TPH adsorption (Li T. et al., 2022).

EPR spectroscopy further confirmed the formation of •OH and $•O_2^-$ during adsorption. DMPO and TEMP were used to capture •OH and $•O_2^-$, as well as $^1O_2$ (Huang W. et al., 2022). As depicted in Figure 6B, PNMSBC showed four DMPO-•OH peaks with a 1:2:2:1 intensity ratio. Moreover, the characteristic signal of superoxide radical was detected, consistent with the free radical quenching results. Furthermore, the expected $^1O_2$ radical signal was not detected, thus indicating that $^1O_2$ radical did not play a certain role in adsorption.

Specific mechanisms for the elimination of TPH by PNMSBC can be proposed based on the above results. The elimination process primarily comprised surface adsorption, oxidation, complexation, and electrostatic interaction. The adsorption capacity of PNMSBC is mainly affected by its specific surface area and oxygen-containing functional groups. SEM shows that the high degree of graphitization is the main reason for the high adsorption capacity of PNMSBC. BET data showed that the larger pore structure and higher pore utilization were the key factors for its rapid adsorption. First, TPH species were transferred from liquid phase to the solid phase of the adsorbent, followed by diffusion on the outer and inner surfaces and pores of PNMSBC, and lastly loaded onto the active site of PNMSBC (Tang et al., 2018). Moreover, after modification with surfactants, the hydrophobicity of PNMSBC is enhanced, which is conducive to adsorption. It could be deduced from FT-IR that the adsorption of petroleum by PNMSBC might be the π-π interaction between the aromatic structure of biochar and aromatic hydrocarbons (Jang and Kan, 2019b). Second, apart from physical forces (e.g., van der Waals forces), hydrophobicity, hydrogen bonds, and steric hindrance, complexation chemically induced PNMSBC for TPH adsorption (Hokkanen et al., 2013). In addition, the positive charge of PNMSBC interacted with the negative charge of TPH in the solution when the pH was below 7.22. In addition to the adsorption of biochar and zero valent iron, the PNMSBC composite also has the effect of reduction and degradation. When the macromolecules of TPH contact with PNMSBC, they can be adsorbed by biochar and surface iron oxides, and then diffuse into the pores of the materials. Then, in the presence of oxygen and water, zero valent iron as an electron donor loses electrons and converts into Fe^{2+} and Fe^{3+}, while the macromolecules of TPH get electrons to break the molecular bonds and convert into small molecular substances, reducing their toxicity and being effectively removed. To be specific, dissolved oxygen in acidic wastewater degraded nZVI, generating Fe^{2+} ions that oxidized to Fe^{3+} ions (Eq. 10–11). Furthermore, the nZVI interacted with dissolved oxygen to produce hydrogen peroxide and Fe^{2+} ions (Eq. 12). The produced hydrogen peroxide interacted with the Fe^{2+} and Fe^{3+} ions, such that the hydroxyl (•OH) and superoxide ($•O_2^-$) radicals were formed (Eq. 13–15) (Zhang L. et al., 2020; Pan et al., 2020). The reaction mechanism is illustrated in Figure 7. As a result, PNMSBC can serve as a

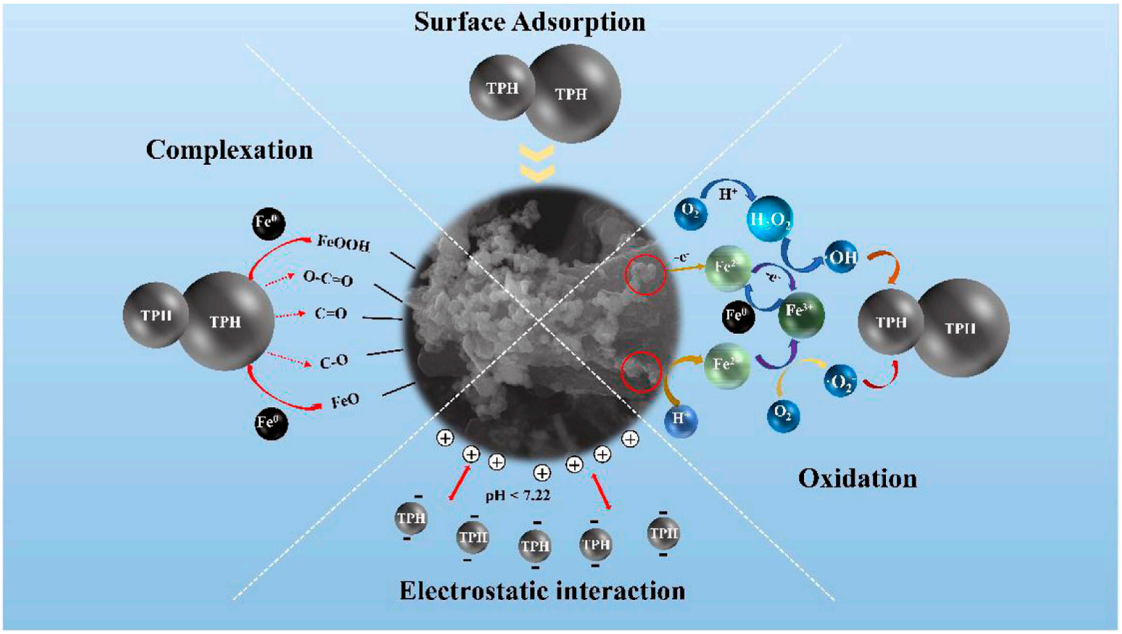

FIGURE 7
Reaction mechanisms of TPH removal by PNMSBC.

new material to eliminate petroleum pollutants and fix TPH pollution in groundwater.

$$2Fe^0 + O_2 + 2H_2O \rightarrow 2Fe^{2+} + 4OH^- \quad (10)$$

$$4Fe^{2+} + 2H_2O + O_2 \rightarrow 4Fe^{3+} + 4OH^- \quad (11)$$

$$Fe^0 + O_2 + 2H^+ \rightarrow Fe^{2+} + H_2O_2 \quad (12)$$

$$Fe^{2+} + H_2O_2 \rightarrow 4Fe^{3+} + \cdot OH + HO^- \quad (13)$$

$$Fe^{2+} + O_2 \rightarrow Fe^{3+} + \cdot O_2^- \quad (14)$$

$$Fe^{2+} + \cdot O_2^- + 2H^+ \rightarrow 2Fe^{3+} + H_2O_2 \quad (15)$$

3.6 Reutilization of MSBC and PNMSBC

Regeneration of adsorption is a crucial metric for determining the adsorption effectiveness of an adsorbent. The adsorption capability of regenerated MSBC and PNMSBC on TPH is presented in Figure 4D. The removal efficiency of TPH as well as the reaction rate gradually decreased with the recycle frequency, which might be the results of byproducts covered on the surface of adsorbent and the loss of Fe^0. After five regeneration studies, the adsorption effect of PNMSBC on TPH was more significant than that of MSBC. The removal rate was higher than 75%. High TPH affinity, π-π interactions, and HCl washing increased difficulties in the full desorption of TPH molecules from the adsorbent. The above results suggest that PNMSBC is stable, effective, and reusable.

4 Conclusion

In this study, KOH-activated biochar loaded PVP and NaOA modified nZVI were employed as an inexpensive catalyst to effectively remove TPH in groundwater. The modified nZVI particles exhibited a smaller particle size, improved dispersion, as well as enhanced TPH adsorption properties. The pseudo-second-order kinetic model and the Freundlich isotherm model more effectively fitted the adsorption experiment data, thus suggesting that the intraparticle diffusion model and liquid film diffusion play a certain role in the adsorption process, with liquid film diffusion as the rate-limiting step. The adsorption capacity of PNMSBC was increased by the abundance of macro and microporous structures. To be specific, a maximum Langmuir adsorption capacity (q_m) was achieved as 75.26 g/g. The result of batch experiments indicated that PNMSBC continuously removed considerable TPH under a wide pH range from 2 to 6, while satisfactory removal results can still be obtained under neutral conditions. Moreover, the TPH sorption was not markedly affected by the bulk of ionic. Besides, the removal effect of TPH increased with the increase of the initial concentration of TPH. After five regeneration studies, the adsorption rate of PNMSBC on TPH was still higher than 75%. The mechanism of removing TPH from an aqueous solution through PNMSBC, surface adsorption, oxidation, complexation, and electrostatic interaction was achieved simultaneously and cooperated to remove TPH from the solution. The above results confirm that unique PNMSBC particles exhibit a substantial catalytic capacity and encourage its vast application for remediating TPH contaminated groundwater.

Data availability statement

The original contributions presented in the study are included in the article/Supplementary Material, further inquiries can be directed to the corresponding authors.

Author contributions

CJ: Investigation, Methodology, Data curation,Writing–original draf. HY: Validation, Data curation. MZ: Conceptualization, Resources, Supervision. ZS: Validation, Investigation, YZ: Supervision, Funding acquisition, Project administration, Writing–review and editing. LL: Resources, Writing–review and editing. All authors contributed to the article and approved the submitted version.

Funding

This study was financially supported by Jiangsu Province Industry-University-Research Cooperation Project (BY2021224), Jiangsu Province major scientific and technological R&D projects (BE2021639), and Postgraduate Research & Practice Innovation Program of Jiangsu Province (KYC22_3106).

Conflict of interest

Authors HY and ZS were employed by Changzhou Keqing Environmental Protection Technology Co., Ltd. Author MZ was employed by Jiangsu Zhongwu Environmental Protection Industry Development Co., Ltd.

The remaining authors declare that the research was conducted in the absence of any commercial or financial relationships that could be construed as a potential conflict of interest.

Publisher's note

Supplementary material

The Supplementary Material for this article can be found online at: https://www.frontiersin.org/articles/10.3389/fmats.2023.1234981/full#supplementary-material

References

Al-Wabel, M. I., Al-Omran, A., El-Naggar, A. H., Nadeem, M., and Usman, A. R. A. (2013). Pyrolysis temperature induced changes in characteristics and chemical composition of biochar produced from conocarpus wastes. *Bioresour. Technol.* 131, 374–379. doi:10.1016/j.biortech.2012.12.165

Arshad, A., Zhang, Z., Zhang, W., and Dilawar, A. (2020). Mapping favorable groundwater potential recharge zones using a GIS-based analytical hierarchical process and probability frequency ratio model: A case study from an agro-urban region of Pakistan. *Geosci. Front.* 11 (5), 1805–1819. doi:10.1016/j.gsf.2019.12.013

Bolade, O. P., Adeniyi, K. O., Williams, A. B., and Benson, N. U. (2021). Remediation and optimization of petroleum hydrocarbons degradation in contaminated water using alkaline activated persulphate. *J. Environ. Chem. Eng.* 9 (4), 105801. doi:10.1016/j.jece.2021.105801

Bubel, S., Mechau, N., and Schmechel, R. (2011). Electronic properties of polyvinylpyrrolidone at the zinc oxide nanoparticle surface PVP in ZnO dispersions and nanoparticulate ZnO thin films for thin film transistors. *J. Mater. Sci.* 46 (24), 7776–7783. doi:10.1007/s10853-011-5757-4

Cai, C., Zhao, M., Yu, Z., Rong, H., and Zhang, C. (2019). Utilization of nanomaterials for *in-situ* remediation of heavy metal(loid) contaminated sediments: A review. *Sci. Total Environ.* 662, 205–217. doi:10.1016/j.scitotenv.2019.01.180

Careghini, A., Saponaro, S., Sezenna, E., Daghio, M., Franzetti, A., Gandolfi, I., et al. (2015). Lab-scale tests and numerical simulations for *in situ* treatment of polluted groundwater, *J. Hazard. Mater.* 287, 162–170. doi:10.1016/j.jhazmat.2015.01.028

Dai, J., Meng, X., Zhang, Y., and Huang, Y. (2020). Effects of modification and magnetization of rice straw derived biochar on adsorption of tetracycline from water. *Bioresour. Technol.* 311, 123455. doi:10.1016/j.biortech.2020.123455

Desalegn, B., Megharaj, M., Chen, Z., and Naidu, R. (2018). Green mango peel-nanozerovalent iron activated persulfate oxidation of petroleum hydrocarbons in oil sludge contaminated soil. *Environ. Technol. Innovation* 11, 142–152. doi:10.1016/j.eti.2018.05.007

Diraki, A., Mackey, H. R., McKay, G., and Abdala, A. (2019). Removal of emulsified and dissolved diesel oil from high salinity wastewater by adsorption onto graphene oxide. *J. Environ. Chem. Eng.* 7 (3), 103106. doi:10.1016/j.jece.2019.103106

Dragan, E. S., Cocarta, A. I., and Dinu, M. V. (2014). Facile fabrication of chitosan/poly(vinyl amine) composite beads with enhanced sorption of Cu2+. Equilibrium, kinetics, and thermodynamics. *Chem. Eng. J.* 255, 659–669. doi:10.1016/j.cej.2014.06.098

Eljamal, R., Eljamal, O., Maamoun, I., Yilmaz, G., and Sugihara, Y. (2020). Enhancing the characteristics and reactivity of nZVI: polymers effect and mechanisms. *J. Mol. Liq.* 315, 113714. doi:10.1016/j.molliq.2020.113714

Gan, C., Liu, Y., Tan, X., Wang, S., Zeng, G., Zheng, B., et al. (2015). Effect of porous zinc-biochar nanocomposites on Cr(VI) adsorption from aqueous solution. *Rsc Adv.* 5 (44), 35107–35115. doi:10.1039/c5ra04416b

Gao, G., Xie, S., Zheng, S., Xu, Y., and Sun, Y. (2022). Two-step modification (sodium dodecylbenzene sulfonate composites acid-base) of sepiolite (SDBS/ABsep) and its performance for remediation of Cd contaminated water and soil. *J. Hazard. Mater.* 433, 128760. doi:10.1016/j.jhazmat.2022.128760

Gong, L., Shi, S., Lv, N., Xu, W., Ye, Z., Gao, B., et al. (2020). Sulfidation enhances stability and mobility of carboxymethyl cellulose stabilized nanoscale zero-valent iron in saturated porous media. *Sci. Total Environ.* 718, 137427. doi:10.1016/j.scitotenv.2020.137427

Hokkanen, S., Repo, E., and Sillanpaa, M. (2013). Removal of heavy metals from aqueous solutions by succinic anhydride modified mercerized nanocellulose. *Chem. Eng. J.* 223, 40–47. doi:10.1016/j.cej.2013.02.054

Huang, J., Yi, S., Zheng, C., and Lo, I. M. C. (2019). Persulfate activation by natural zeolite supported nanoscale zero-valent iron for trichloroethylene degradation in groundwater. *Sci. Total Environ.* 684, 351–359. doi:10.1016/j.scitotenv.2019.05.331

Huang, J., Zhao, D., Zhao, Y., Tu, Y., and Wang, R. (2022a). Polyvinylpyrrolidone supported nZVI/Ni bimetallic nanoparticles for enhanced high-performance removal of aqueous Cr(VI). *Chem. Phys. Lett.* 791, 139375. doi:10.1016/j.cplett.2022.139375

Huang, W., Tang, Y., Zhang, X., Luo, Z., and Zhang, J. (2022b). nZVI-biochar derived from Fe3O4-loaded rabbit manure for activation of peroxymonosulfate to degrade sulfamethoxazole. *J. Water Process Eng.* 45, 102470. doi:10.1016/j.jwpe.2021.102470

Hussain, I., Li, M., Zhang, Y., Li, Y., Huang, S., Du, X., et al. (2017). Insights into the mechanism of persulfate activation with nZVI/BC nanocomposite for the degradation of nonylphenol. *Chem. Eng. J.* 311, 163–172. doi:10.1016/j.cej.2016.11.085

Idrees, A., Shan, A., Ali, M., Abbas, Z., Shahzad, T., Hussain, S., et al. (2021). Highly efficient degradation of trichloroethylene in groundwater based on persulfate activation by polyvinylpyrrolidone functionalized Fe/Cu bimetallic nanoparticles. *J. Environ. Chem. Eng.* 9 (4), 105341. doi:10.1016/j.jece.2021.105341

Jang, H. M., and Kan, E. (2019a). A novel hay-derived biochar for removal of tetracyclines in water. *Bioresour. Technol.* 274, 162–172. doi:10.1016/j.biortech.2018.11.081

Jang, H. M., and Kan, E. (2019b). Engineered biochar from agricultural waste for removal of tetracycline in water. *Bioresour. Technol.* 284, 437–447. doi:10.1016/j.biortech.2019.03.131

Jing, H., Zhan, M. J., and lei, Z. (2016). Study on treating O-dichlorobenzene in groundwater with permeable reactive barrier. *Environ. Sci. Technol.* 29 (5), 31–33. doi:10.19674/j.cnki.issn20161008.1623.004

Lefevre, E., Bossa, N., Wiesner, M. R., and Gunsch, C. K. (2016). A review of the environmental implications of *in situ* remediation by nanoscale zero valent iron (nZVI): behavior, transport and impacts on microbial communities. *Sci. Total Environ.* 565, 889–901. doi:10.1016/j.scitotenv.2016.02.003

Li, S., Yang, F., Li, J., and Cheng, K. (2020). Porous biochar-nanoscale zero-valent iron composites: synthesis, characterization and application for lead ion removal. *Sci. Total Environ.* 746, 141037. doi:10.1016/j.scitotenv.2020.141037

Li, R., Xiao, X., Zhao, Y., Tu, B., and Zhu, X. (2022a). Characteristics of the archaeal communities in petroleum hydrocarbon-contaminated groundwater. *Water Air Soil Pollut.* 233 (3), 69. doi:10.1007/s11270-022-05544-6

Li, Y., Li, S., Hu, B., Zhao, X., and Guo, P. (2022b). FeOOH and nZVI combined with superconducting high gradient magnetic separation for the remediation of high-arsenic metallurgical wastewater. *Sep. Purif. Technol.* 285, 120372. doi:10.1016/j.seppur.2021.120372

Li, Y., Wen, J., Xue, Z., Yin, X., Yuan, L., and Yang, C. (2022c). Removal of Cr(VI) by polyaniline embedded polyvinyl alcohol/sodium alginate beads-Extension from water treatment to soil remediation. *J. Hazard. Mater.* 426, 127809. doi:10.1016/j.jhazmat.2021.127809

Li, T., Cui, P., Wang, X., Liu, C., Zeng, Y., Fang, G., et al. (2022d). Efficient activation of peroxymonosulfate by C3N5 doped with cobalt for organic contaminant degradation. *Environ. Science-Nano* 9, 2534–2547. doi:10.1039/d2en00216g

Liu, X., Lai, D., and Wang, Y. (2019). Performance of Pb(II) removal by an activated carbon supported nanoscale zero-valent iron composite at ultralow iron content. *J. Hazard. Mater.* 361, 37–48. doi:10.1016/j.jhazmat.2018.08.082

Liu, K., Li, F. B., Tian, Q. W., Nie, C. R., Ma, Y. B., Zhu, Z. L., et al. (2021). A highly porous animal bone-derived char with a superiority of promoting nZVI for Cr(VI) sequestration in agricultural soils. *J. Environ. Sci.* 104, 27–39. doi:10.1016/j.jes.2020.11.031

Liu, H., Hu, M., Zhang, H., and Wei, J. (2022a). Biosynthesis of stalk Biochar-nZVI and its catalytic reactivity in degradation of dyes by persulfate. *Surfaces Interfaces* 31, 102098. doi:10.1016/j.surfin.2022.102098

Liu, T., Wang, P., and Wang, Z.-L. (2022b). A high-efficient and recyclable aged nanoscale zero-valent iron compound for V5+ removal from wastewater: characterization, performance and mechanism. *Chemosphere* 302, 134833. doi:10.1016/j.chemosphere.2022.134833

Ma, B., Yao, J., Chen, Z., Liu, B., Kim, J., Zhao, C., et al. (2022). Superior elimination of Cr(VI) using polydopamine functionalized attapulgite supported nZVI composite: behavior and mechanism. *Chemosphere* 287, 131970. doi:10.1016/j.chemosphere.2021.131970

Mittal, A., Thakur, V., and Gajbe, V. (2012). Evaluation of adsorption characteristics of an anionic azo dye Brilliant Yellow onto hen feathers in aqueous solutions. *Environ. Sci. Pollut. Res.* 19 (6), 2438–2447. doi:10.1007/s11356-012-0756-9

Moslemy, P., Guiot, S. R., and Neufeld, R. J., Production of size-controlled gellan gum microbeads encapsulating gasoline-degrading bacteria, *Enzyme Microb. Technol.* 30(1) (2002) 10–18.doi:10.1016/S0141-0229(01)00440-9

Neeli, S. T., and Ramsurn, H., Synthesis and formation mechanism of iron nanoparticles in graphitized carbon matrices using biochar from biomass model compounds as a support, *Carbon* 134 (2018) 480–490.doi:10.1016/j.carbon.2018.03.079

Ogawa, T., and Kawase, Y. (2021). Effect of solution pH on removal of anionic surfactant sodium dodecylbenzenesulfonate (SDBS) from model wastewater using nanoscale zero-valent iron (nZVI). *J. Environ. Chem. Eng.* 9 (5), 105928. doi:10.1016/j.jece.2021.105928

Pan, Y., Bu, Z., Sang, C., Guo, H., Zhou, M., Zhang, Y., et al. (2020). EDTA enhanced pre-magnetized Fe-0/H2O2 process for removing sulfamethazine at neutral pH. *Sep. Purif. Technol.* 250, 117281. doi:10.1016/j.seppur.2020.117281

Phenrat, T., Long, T. C., Lowry, G. V., and Veronesi, B. (2009). Partial oxidation ("Aging") and surface modification decrease the toxicity of nanosized zerovalent iron. *Environ. Sci. Technol.* 43 (1), 195–200. doi:10.1021/es801955n

Phenrat, T., Thongboot, T., and Lowry, G. V. (2016). Electromagnetic induction of zerovalent iron (ZVI) powder and nanoscale zerovalent iron (NZVI) particles enhances dechlorination of trichloroethylene in contaminated groundwater and soil: proof of concept. *Environ. Sci. Technol.* 50 (2), 872–880. doi:10.1021/acs.est.5b04485

Poi, G., Shahsavari, E., Aburto-Medina, A., Mok, P. C., and Ball, A. S. (2018). Large scale treatment of total petroleum-hydrocarbon contaminated groundwater using bioaugmentation. *J. Environ. Manag.* 214, 157–163. doi:10.1016/j.jenvman.2018.02.079

Qin, Y., Chai, B., Wang, C., Yan, J., Fan, G., and Song, G. (2022). Removal of tetracycline onto KOH-activated biochar derived from rape straw: affecting factors, mechanisms and reusability inspection. *Colloids Surfaces a-Physicochemical Eng. Aspects* 640, 128466. doi:10.1016/j.colsurfa.2022.128466

Qiu, X., Fang, Z., Liang, B., Gu, F., and Xu, Z. (2011). Degradation of decabromodiphenyl ether by nano zero-valent iron immobilized in mesoporous silica microspheres. *J. Hazard. Mater.* 193, 70–81. doi:10.1016/j.jhazmat.2011.07.024

Qu, J., Wang, Y., Tian, X., Jiang, Z., Deng, F., Tao, Y., et al. (2021). KOH-activated porous biochar with high specific surface area for adsorptive removal of chromium (VI) and naphthalene from water: affecting factors, mechanisms and reusability exploration. *J. Hazard. Mater.* 401, 123292. doi:10.1016/j.jhazmat.2020.123292

Sakulchaicharoen, N., O'Carroll, D. M., and Herrera, J. E. (2010). Enhanced stability and dechlorination activity of pre-synthesis stabilized nanoscale FePd particles. *J. Contam. Hydrology* 118 (3-4), 117–127. doi:10.1016/j.jconhyd.2010.09.004

Sarathy, V., Tratnyek, P. G., Nurmi, J. T., Baer, D. R., Amonette, J. E., Chun, C. L., et al. (2008). Aging of iron nanoparticles in aqueous solution: effects on structure and reactivity. *J. Phys. Chem. C* 112 (7), 2286–2293. doi:10.1021/jp0777418

Shang, J., Zong, M., Yu, Y., Kong, X., Du, Q., and Liao, Q. (2017). Removal of chromium (VI) from water using nanoscale zerovalent iron particles supported on herb-residue biochar. *J. Environ. Manag.* 197, 331–337. doi:10.1016/j.jenvman.2017.03.085

Smith, M. J., Flowers, T. H., Duncan, H. J., and Alder, J. (2006). Effects of polycyclic aromatic hydrocarbons on germination and subsequent growth of grasses and legumes in freshly contaminated soil and soil with aged PAHs residues. *Environ. Pollut.* 141 (3), 519–525. doi:10.1016/j.envpol.2005.08.061

Su, H., Fang, Z., Tsang, P. E., Fang, J., and Zhao, D. (2016). Stabilisation of nanoscale zero-valent iron with biochar for enhanced transport and *in-situ* remediation of hexavalent chromium in soil. *Environ. Pollut.* 214, 94–100. doi:10.1016/j.envpol.2016.03.072

Sun, Y.-P., Li, X.-q., Cao, J., Zhang, W.-x., and Wang, H. P. (2006). Characterization of zero-valent iron nanoparticles. *Adv. Colloid Interface Sci.* 120 (1-3), 47–56. doi:10.1016/j.cis.2006.03.001

Takeuchi, T., Sarashina, I., Iijima, M., and Endo, K. (2008). *In vitro* regulation of CaCO3 crystal polymorphism by the highly acidic molluscan shell protein Aspein. *Febs Lett.* 582 (5), 591–596. doi:10.1016/j.febslet.2008.01.026

Tang, L., Yu, J., Pang, Y., Zeng, G., Deng, Y., Wang, J., et al. (2018). Sustainable efficient adsorbent: alkali-acid modified magnetic biochar derived from sewage sludge for aqueous organic contaminant removal. *Chem. Eng. J.* 336, 160–169. doi:10.1016/j.cej.2017.11.048

Tian, H., Liang, Y., Yang, D., and Sun, Y. (2020). Characteristics of PVP-stabilised NZVI and application to dechlorination of soil-sorbed TCE with ionic surfactant. *Chemosphere* 239, 124807. doi:10.1016/j.chemosphere.2019.124807

Tosco, T., Papini, M. P., Viggi, C. C., and Sethi, R. (2014). Nanoscale zerovalent iron particles for groundwater remediation: A review. *J. Clean. Prod.* 77, 10–21. doi:10.1016/j.jclepro.2013.12.026

Wang, T., Su, J., Jin, X., Chen, Z., Megharaj, M., and Naidu, R. (2013). Functional clay supported bimetallic nZVI/Pd nanoparticles used for removal of methyl orange from aqueous solution. *J. Hazard. Mater.* 262, 819–825. doi:10.1016/j.jhazmat.2013.09.028

Wang, J., Liu, D., Huang, Z., and Zheng, C. (2018). CO2 responsive wormlike micelles based on sodium oleate, potassium chloride and N,N-dimethylethanolamine. *J. Dispersion Sci. Technol.* 39 (11), 1606–1612. doi:10.1080/01932691.2018.1452758

Wang, Z., Xu, J., Yellezuome, D., and Liu, R. (2021). Effects of cotton straw-derived biochar under different pyrolysis conditions on Pb (II) adsorption properties in aqueous solutions. *J. Anal. Appl. Pyrolysis* 157 (1), 105214. doi:10.1016/j.jaap.2021.105214

Wu, Y., Yue, Q., Ren, Z., and Gao, B. (2018). Immobilization of nanoscale zero-valent iron particles (nZVI) with synthesized activated carbon for the adsorption and degradation of Chloramphenicol (CAP). *J. Mol. Liq.* 262, 19–28. doi:10.1016/j.molliq.2018.04.032

Xu, C., Yang, W., Liu, W., Sun, H., Jiao, C., and Lin, A.-j. (2018). Performance and mechanism of Cr(VI) removal by zero-valent iron loaded onto expanded graphite. *J. Environ. Sci.* 67, 14–22. doi:10.1016/j.jes.2017.11.003

Xu, J., Zhang, Y., Li, B., Fan, S., Xu, H., and Guan, D.-X. (2022). Improved adsorption properties of tetracycline on KOH/KMnO4 modified biochar derived from wheat straw. *Chemosphere* 296, 133981. doi:10.1016/j.chemosphere.2022.133981

Yang, D.-S., and Chen, S.-T. (2020). Use of a novel biopellet to treat total petroleum hydrocarbon contaminated groundwater. *Water* 12 (9), 2512. doi:10.3390/w12092512

Yu, P., Liping, S., Chan, G., and mingyi, L. (2019). Removal of 2,4-dichlorophenol from groundwater by PRB simulated by CMC modified nanoscale Fe/Cu bimetal. *China Environ. Sci.* 39 (9), 3789–3796. doi:10.19674/j.cnki.issn1000-6923.2019.0445

Yuanyuan, L., Zhang, L., and mingying, Q. (2012). Study on reductive dechlorination of PCBs in groundwater by Fe/Zn bimetal. *J. Anhui Agri*, 8673–8676.

Zeng, Z., Ye, S., Wu, H., Xiao, R., Zeng, G., Liang, J., et al. (2019). Research on the sustainable efficacy of g-MoS2 decorated biochar nanocomposites for removing tetracycline hydrochloride from antibiotic-polluted aqueous solution. *Sci. Total Environ.* 648, 206–217. doi:10.1016/j.scitotenv.2018.08.108

Zeng, H., Hao, H., Wang, X., and Shao, Z. (2022). Chitosan-based composite film adsorbents reinforced with nanocellulose for removal of Cu(II) ion from wastewater: preparation, characterization, and adsorption mechanism. *Int. J. Biol. Macromol.* 213, 369–380. doi:10.1016/j.ijbiomac.2022.05.103

Zhang, S., Du, Q., Cheng, K., Antonietti, M., and Yang, F. (2020a). Efficient phosphorus recycling and heavy metal removal from wastewater sludge by a novel hydrothermal humification-technique. *Chem. Eng. J.* 394, 124832. doi:10.1016/j.cej.2020.124832

Zhang, L., Wu, B., Gan, Y., Chen, Z., and Zhang, S. (2020b). Sludge reduction and cost saving in removal of Cu(II)-EDTA from electroplating wastewater by introducing a low

dose of acetylacetone into the Fe(III)/UV/NaOH process. *J. Hazard. Mater.* 382, 121107. doi:10.1016/j.jhazmat.2019.121107

Zhao, X., Liu, W., Cai, Z., Han, B., Qian, T., and Zhao, D. (2016). An overview of preparation and applications of stabilized zero-valent iron nanoparticles for soil and groundwater remediation. *Water Res.* 100, 245–266. doi:10.1016/j.watres.2016.05.019

Zhao, L., Zhao, Y., Yang, B., and Teng, H. (2019). Application of carboxymethyl cellulose-stabilized sulfidated nano zerovalent iron for removal of Cr(VI) in simulated groundwater. *Water Air Soil Pollut.* 230 (6), 113. doi:10.1007/s11270-019-4166-1

Zhou, Q., and Hu, X. (2017). Systemic stress and recovery patterns of rice roots in response to graphene oxide nanosheets. *Environ. Sci. Technol.* 51 (4), 2022–2030. doi:10.1021/acs.est.6b05591

Zhu, C., Zhu, F., Dionysiou, D. D., Zhou, D., Fang, G., and Gao, J. (2018). Contribution of alcohol radicals to contaminant degradation in quenching studies of persulfate activation process. *Water Res.* 139, 66–73. doi:10.1016/j.watres.2018.03.069

Zhu, L., Tong, L., Zhao, N., Li, J., and Lv, Y. (2019). Coupling interaction between porous biochar and nano zero valent iron/nano alpha-hydroxyl iron oxide improves the remediation efficiency of cadmium in aqueous solution. *Chemosphere* 219, 493–503. doi:10.1016/j.chemosphere.2018.12.013